



Universiteit
Leiden
The Netherlands

Re-evaluation of Lunar X-ray observations by Apollo 15 and 16

Gloude-mans, A.J.; Kuulkers, E.; Campana, R.; Escalante, A.; Kole, M.; Mollard, Y.

Citation

Gloude-mans, A. J., Kuulkers, E., Campana, R., Escalante, A., Kole, M., & Mollard, Y. (2021). Re-evaluation of Lunar X-ray observations by Apollo 15 and 16. *Astronomy & Astrophysics*, 649. doi:10.1051/0004-6361/202140321

Version: Accepted Manuscript

License: [Leiden University Non-exclusive license](#)

Downloaded from: <https://hdl.handle.net/1887/3250949>

Note: To cite this publication please use the final published version (if applicable).

Re-evaluation of Lunar X-ray observations by Apollo 15 & 16^{*}

A. J. Gloudemans^{1,2,3}, E. Kuulkers¹, R. Campana⁴, A. Escalante⁵, M. Kole⁶, and Y. Mollard⁷

¹ ESA/ESTEC, Keplerlaan 1, 2201 AZ Noordwijk, The Netherlands

² Anton Pannekoek Institute for Astronomy, University of Amsterdam, Science Park 904, 1098 XH, Amsterdam, The Netherlands

³ Leiden Observatory, Leiden University, PO Box 9513, 2300 RA Leiden, The Netherlands
e-mail: gloudemans@strw.leidenuniv.nl

⁴ INAF/OAS, Via Gobetti 101, I-40129, Bologna, Italy

⁵ ESA/ESAC, Camino Bajo del Castillo, 28692 Villafranca del Castillo, Madrid, Spain

⁶ Department of Nuclear and Particle Physics, University of Geneva, 24 quai Ernest-Ansermet, 1205, Geneva, Switzerland

⁷ Bordeaux INP, Avenue des facultés, 33405 Talence, France

Received 12 January 2021 / Accepted 16 April 2021

ABSTRACT

The Apollo 15 & 16 missions were the first to explore the Lunar surface chemistry by investigating about 10% of the Lunar surface using a remote sensing X-ray fluorescence spectrometer experiment. The data obtained have been extensively used to study Lunar formation history and geological evolution. In this work, a re-evaluation of the Apollo 15 & 16 X-ray fluorescence experiment is conducted with the aim of obtaining up-to-date empirical values for aluminum (Al) and magnesium (Mg) concentrations relative to silicon (Si) of the upper Lunar surface. An updated instrument response, a newly reconstructed Lunar trajectory orbit, and improved intensity ratio calculations were used to obtain new intensity ratio maps. The resulting Lunar Al/Si and Mg/Al X-ray maps show a clear distinction in Lunar mare and highland regions. The mean Al/Si and Mg/Al intensity ratios for the mare regions obtained from the newly obtained maps are 0.54 ± 0.07 and 0.54 ± 0.17 , respectively; for the highland regions, the values are 0.76 ± 0.07 and 1.07 ± 0.13 , respectively. For the Mg/Si intensity ratio, no clear distinction between Lunar features is obtained and we derived a mean value of 0.47 ± 0.13 . Our determined intensity ratios are lower than previously published. These values can be used to infer concentration ratios when accounting for Solar activity, inter-orbit variability, and measurements from different instruments. We employed a correction to infer concentration ratios by comparing our intensity ratios directly to Lunar rock concentrations obtained from various Lunar missions.

Key words. Moon - X-rays: general - Planets and satellites: surfaces - Space vehicles: instruments

1. Introduction

The Apollo 15 & 16 spacecrafts were launched on July 26, 1971 and April 16, 1972, respectively. The Lunar orbiting spacecraft (Command Service Module, CSM) on both missions carried out an X-ray fluorescence spectrometer (XRFS) experiment (Adler et al. 1972a; Adler et al. 1975; Jagoda et al. 1974) within the Scientific Instrumentation Module (SIM), which was used for Lunar surface exploration. X-ray spectroscopy is of high importance for geochemical exploration of the Moon and other bodies, such as planets and asteroids, as it can be used to study extended surface areas, without having to land on their surfaces. X-rays can be observed via fluorescence and scattering of Solar X-rays on a body's surface. Solar X-rays reaching the Lunar surface excite electrons in medium to high atomic number elements (such as aluminum), which in turn emit characteristic X-rays from the specific element. The chemical composition of the surface can give information on, for example, the formation history of the body or crater impact events. The Apollo 15 & 16 missions were the first to use an XRFS experiment in orbit (see, e.g., Clark & Trombka 1997) and also the first to investigate a large part (~10%) of the Lunar surface. These measurements were the basic ingredient of our early understanding of the ge-

ology and formation of the Lunar surface. Also more recent Lunar missions such as SMART-1/D-C1XS (Racca et al. 2001; Foning et al. 2006), Chandryaan 1/C1XS (Narendranath et al. 2011), and Chang'E-2/CE2XRS (Dong et al. 2016) have since used orbital X-ray fluorescence spectroscopy to study the Lunar surface. Moreover, X-ray telescopes, such as ROSAT (Schmitt et al. 1991), ASCA (Kamata et al. 1999), and Chandra (Wargelin et al. 2004), have also observed the Lunar surface. In addition to this, fluorescence spectroscopy has been used in studies of, for example, Mercury by MESSENGER/XRS (Schlemm et al. 2007; Nittler et al. 2011; Weider et al. 2015) and other Solar system moons and asteroids (e.g., 433 Eros, Nittler et al. 2001, and asteroid Itokawa, Okada et al. 2007).

In this work, a re-evaluation of the Apollo 15 & 16 XRFS experiment data is performed using an updated instrument response, a newly reconstructed Lunar trajectory orbit, and improved intensity ratio calculations. The data are not only of historical value, but doing the re-evaluation now also enables us to compare the results with those of much later X-ray fluorescent experiments (such as with the Chandryaan-1/C1XS) and up-to-date Lunar sample analyses. Our primary aim is to create chemical intensity ratio maps of measured elements, such as aluminum (Al) and magnesium (Mg) with respect to silicon (Si), on the Lunar surface using newly obtained values and make a comparison with inferred elemental concentrations found in Lunar rocks.

^{*} This work is dedicated to Al(fred Merrill) Worden †, who operated the XRFS instrument during the Lunar orbit of the Apollo 15 mission.

2. Apollo 15 and 16 X-ray observations

2.1. XRFS instrument

The XRFS instrument consisted of three detectors and a Solar monitor, which were all proportional counters. The proportional counters were filled with 90% argon (Ar), 9.5% carbon dioxide (CO₂), and 0.5% helium (He). All three detectors had a beryllium (Be) window with a thickness of approximately 25 μm (e.g., Adler et al. 1972a) and each detector had an effective window area of about 25 cm².

One detector had no filter (referred to as Detector #1), whereas the other two detectors had an Mg (Detector #2) and an Al filter (Detector #3), respectively, in front of their windows. The thickness of the Mg and Al filters, as well as that of the Be windows, is not entirely clear from the literature as different values have been published (compare, e.g., Adler et al. 1972a; Adler et al. 1975; Yin et al. 1993). An overview of these different values and the implication thereof is discussed in Appendix A. We assume that the Mg and Al foils have a thickness of 5.1 and 6.4 μm , respectively (e.g., Yin et al. 1993). The different filters provided selective filtering of the elements Si, Al, and Mg (see, e.g., Clark & Trombka 1997) since the energy resolution of the individual proportional counters could not adequately separate the Si, Al, and Mg lines. The field-of-view (FOV) of the detectors were set by collimator cells placed in front of the three detectors, which resulted in a FOV of approximately $\pm 30^\circ$ at full-width at half maximum (see Adler et al. 1975). A sample analysis shows the collimator is presumably made of Cu-Zn alloy (Kuulkers et al. in prep).

The data handling system recorded the X-ray photons in eight spectral channels. The XRFS was able to operate in a normal mode and extended mode. In normal mode, the first seven channels of all detectors covered an energy range of 0.69–3.0 keV. Channel 8 covered all energies higher than 3.0 keV (Jagoda et al. 1974). In the extended mode, each channel energy range of Detector 1 was doubled. In both modes, each detector output was read out every 8 seconds. The gain, resolution, and efficiency of the detectors were calibrated by using in-flight calibration sources consisting of radioactive sources ⁵⁵Fe and Mn-K _{α} . Calibration measurements were done every 16 minutes for a duration of 64 seconds.

The Solar monitor simultaneously measured the Sun's X-ray output with the detectors observing the Lunar surface: It was placed at the other side of the CSM with respect to the three detectors. The Apollo 15 Solar monitor had one Be window, while the Apollo 16 Solar monitor had two Be windows. The extra Be filter was added for the Apollo 16 mission because the detector experienced gain shifts during the Apollo 15 flight (Adler et al. 1972b). For further details on the XRFS instrument, we refer readers to Adler et al. (1972a), Jagoda et al. (1974), and Adler et al. (1975).

2.2. Lunar surface observations

The Apollo 15 and 16 XRFS observations were performed during 5.7 and 4.7 days in Lunar orbit, respectively (see Tab. 1), and together they measured $\sim 10\%$ of the Lunar surface (see, e.g., Yin et al. 1993). The XRFS instrument operated in normal mode for $\sim 75\%$ of the time and the remaining time in extended mode. We retrieved the Apollo 15 and 16 X-ray data from the Planetary Data System (PDS) at the NASA Space Science Data Coordinated (NSSDC) Archive. For each mission, the data sets contain ASCII tables of time-ordered, raw event count rates acquired by

the XRFS from July 30 to August 4, 1971 (Apollo 15; Adler et al. 2007) and from April 20 to 24, 1972 (Apollo 16; Trombka et al. 2007) during Lunar orbit.

The Apollo 15 trans-Earth coast XRFS data as well as the full Apollo 15 and 16 merged data sets from the Gamma-Ray Spectrometer (GRS; Harrington et al. 1974) were available as restored binary offline tape data sets at the NSSDC Archive and deciphered by us. The trajectory information stored in the data from the GRS was used to reconstruct, with high accuracy, the orbit of the CSM, propagating the positions and velocities expressed in the inertial frame B1950, centered on the Moon. Given the CSM position and velocity computed from the propagation of the GRS data, the transformation from the B1950 inertial reference frame to the local horizontal reference frame can be computed at the times of the XRFS measurements for which the body angles are also known. Then, using the Euler angles from the XRFS tape to transform from local horizontal to body-fixed, the attitude of the CSM is unequivocally defined.

During the Lunar orbit, the CSM continuously changed altitude. The CSM was in a low-altitude orbit (~ 20 – 100 km) during the first part of both Apollo missions and in a higher-altitude orbit (~ 100 – 120 km) during the second part.

2.3. Data processing

Intensity ratios of measured Al, Si, and Mg intensities were used to eliminate effects of non-geochemical variations such as the Solar illumination angle and Lunar surface roughness (e.g., Adler et al. 1972a). These intensity ratios are Al/Si, Mg/Si, and Mg/Al. The Si abundance on the Lunar surface is high and stable, changing only by a maximum of 5% across the surface, hence the ratios are mostly a measure of the Al and Mg variation, and concentration, on the Lunar surface (e.g., Yin et al. 1993).

We made multiple assumptions when examining the data. Firstly, 100% efficiency of the proportional counter was assumed, that is, all X-rays that enter the proportional counter are absorbed by the argon gas and give rise to an X-ray detection (see e.g., Yin et al. 1993). Secondly, it was assumed that the three detectors have identical characteristics except for their filters (see, e.g., Adler et al. 1972a). For example, the seven spectral channels of each detector of both Apollo missions cover the same energy range of 0.69–3.0 keV in normal mode (Jagoda et al. 1974).

In the first step of data processing, the data obtained during calibration periods were removed (see also Adler et al. 2007; Trombka et al. 2007). The contribution due to background radiation was determined from the XRFS observations in Lunar orbit ~ 30 – 150 degrees away from the sub-Solar point. The background was determined for each detector and each spectral channel independently and subtracted from the detector channel count rates.

During Apollo 16, the Solar spectrum was softer than during the Apollo 15 mission (Bielefeld 1977). The softening of the Solar spectrum caused a decrease in excitation of Si compared to Al and Mg during Apollo 16 since Si has a higher atomic number. We corrected the Apollo 16 observations for that effect (see Sect. 2.4). Also, during several orbits of both missions, the Solar activity was higher than usual (e.g., revolution 67 of Apollo 15, see Adler et al. 1972a), causing enhanced excitation of Si. These orbits were removed from the data in our analysis (see Sect. 2.4).

To determine the characteristic line intensities of Mg, Al, and Si, the transmission as a function of energy of each filter has to be taken into account. The expression for transmission can be

Table 1: Log of the observations with the XRFS onboard Apollo 15 & 16 in normal and extended mode of Detector #1.

		Date start observation (UTC)	Date end observation (UTC)	Total exposure time (h)
Apollo 15	Normal mode	30 Jul 1971 02:44:07	04 Aug 1971 18:21:48	54.62
	Extended mode	30 Jul 1971 08:09:10	04 Aug 1971 12:40:55	14.78
Apollo 16	Normal mode	20 Apr 1972 01:58:03	24 Apr 1972 17:47:31	50.00
	Extended mode	20 Apr 1972 07:45:15	24 Apr 1972 19:24:22	14.52

Table 2: Absorption cross section, density, and filter thickness of the Mg, Al, and Be filter at $K\alpha$ line energies of Mg, Al, and Si. The filter thickness is adopted from Yin et al. (1993). Absorption cross sections were determined using the web tool *xraylib* (Schoonjans et al. 2011).

Element	Absorption cross section μ (cm^2g^{-1})			ρ (g cm^{-3})	d (μm)
	1.254 keV (Mg)	1.487 keV (Al)	1.740 keV (Si)		
Be	307.76	184.47	114.47	1.84	25.4
Mg	502.39	4084.09	2782.42	1.74	5.1
Al	648.13	411.68	3111.63	2.70	6.4

written as follows (see Adler et al. 1972a):

$$G_i = \sum_{j=1}^3 I_j^T T_j^{Be} F_{ij}, \quad (1)$$

where G_i is the total photon counts in detector i ; I_j^T is the total X-ray intensity at energy j for the Mg, Al, and Si line; T_j^{Be} is the X-ray transmission efficiency of the Be detector window; and F_{ij} are the filter transmission efficiencies of the Mg and Al filters for energy j . The intensity received by Detectors #1, #2, and #3 is given by the following:

$$I_1 = I'_1 e^{-(\mu_{Be}\rho_{Be}d_{Be})}, \quad (2)$$

$$I_2 = I'_2 e^{-(\mu_{Be}\rho_{Be}d_{Be} + \mu_{Mg}\rho_{Mg}d_{Mg})}, \quad (3)$$

$$I_3 = I'_3 e^{-(\mu_{Be}\rho_{Be}d_{Be} + \mu_{Al}\rho_{Al}d_{Al})}, \quad (4)$$

with I'_i being the incident intensity, μ being the absorption cross section of the specific element in cm^2g^{-1} , ρ being the density in g cm^{-3} , and d being the thickness of the filter in centimeters. The transmission factors are subsequently given by I/I' and can be determined at the Mg, Al, and Si $K\alpha$ lines at 1.254, 1.487, and 1.740 keV, respectively. Nowadays, the absorption cross section for different elements are accurately determined (e.g., Schoonjans et al. 2011). We used these absorption cross-section values, which are given in Tab. 2, together with the filter thicknesses and densities in the calculations. This is in contrast to previous work (e.g., Clark & Trombka 1997) where power laws were used to determine the mass absorption. Subsequently, a "filter matrix" M was constructed to finally obtain the intensity ratios of Al/Si, Mg/Si, and Mg/Al, which is further explained in Appendix B.

The collimator transmission has been described by Golub et al. (1972), Adler et al. (1975), and Bielefeld et al. (1977). When re-engineering the dimensions of the various parts of the XRFS from these reports, it became apparent that the transmissions shown in these reports could not be reproduced. Also, the re-engineered values did not match what was expected from in-flight measurements of the various X-ray sources observed during the trans-Earth coast of Apollo 15. A prototype unit of the XRFS still exists; using the dimensions of the detector assembly from this unit, the results from in-flight measurements can be reproduced, and an updated collimator transmission can be derived (Kuulkers et al., in preparation).

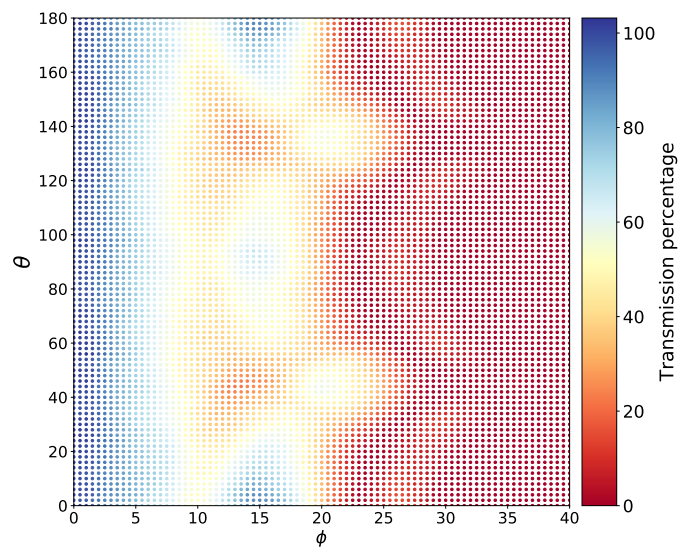


Fig. 1: Collimator response (0–100%) for angles of $0^\circ < \phi < 40^\circ$ and $0^\circ < \theta < 180^\circ$. The angles ϕ and θ represent the geometric off-axis sighting angles on the detector (see Golub et al. 1972, Adler et al. 1975).

The collimator transmission values (Fig. 1) were obtained by implementing a Monte Carlo simulation. The angles ϕ and θ represent the geometric off-axis sighting angles on the detector (see Golub et al. 1972; Adler et al. 1975). The Monte Carlo simulation involved a geometrical mass model of the XRFS experiment, using the Geant4 framework. Geant4 (Agostinelli et al. 2003) is a tool kit for the simulation of the passage of particles through matter, with a large set of applications in high-energy, nuclear, accelerator, medical, and space-science physics, and it is routinely used to estimate the response of space astrophysics instrumentation. For the work presented here, version 4.10.2 of Geant4 was used with the LivermorePhysics model handling the electromagnetic process including fluorescence effects. The various parameters of the collimator and detector unit (dimensions, thicknesses) were adapted using the measurements on the prototype unit.

The response was derived by simulating 1×10^6 incident photons for 100 different incoming energies, ranging from 0.1 to 10

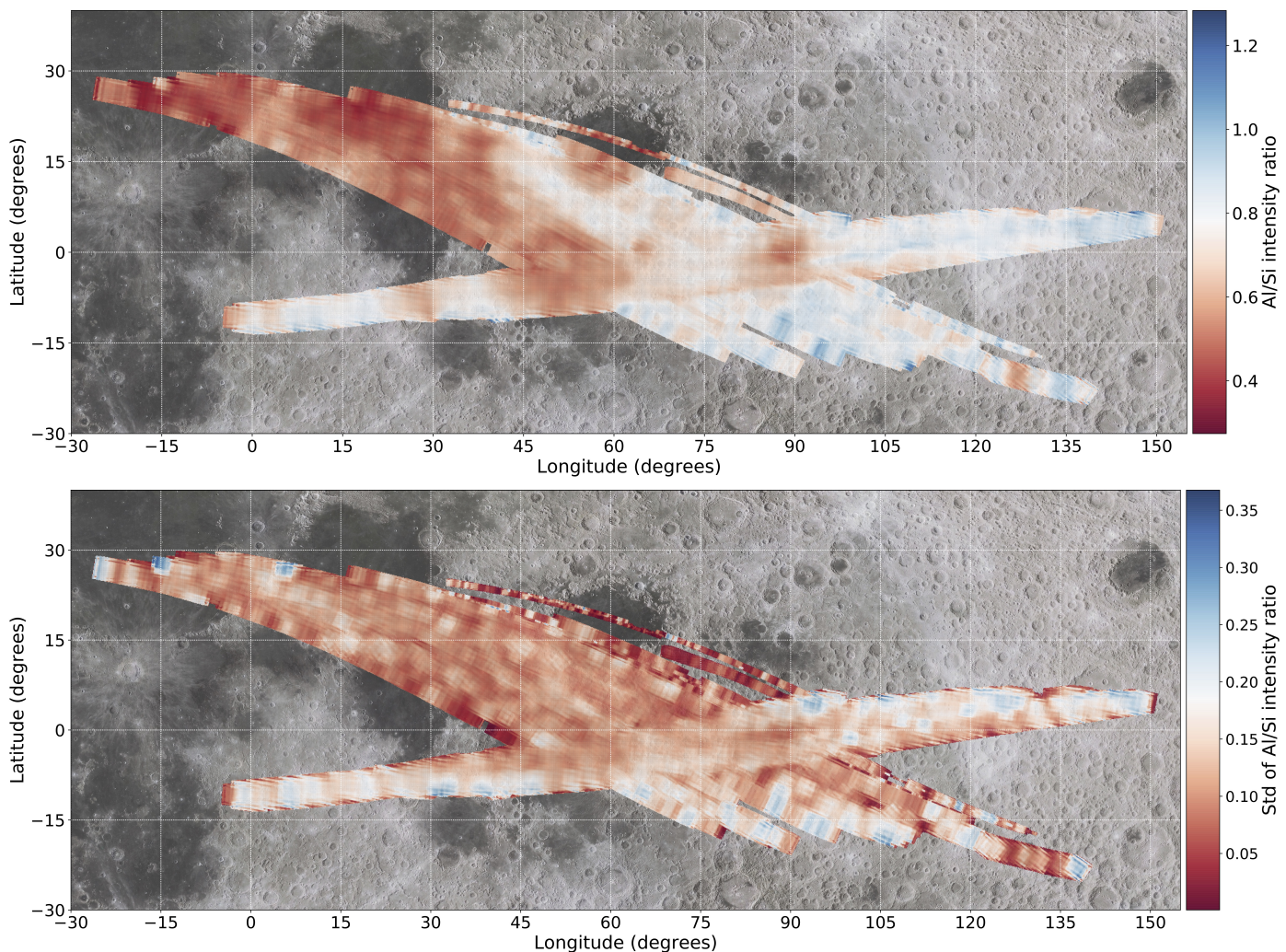


Fig. 2: Map of Al/Si intensity ratio (top panel) and standard deviation (bottom panel) measured by the Apollo 15 and 16 XRFs projected onto an optical image of the Lunar surface. Background image credit: NASA (www.Solarsystemscope.com/textures/).

keV in 0.1 keV steps, coming from different sighting directions in the (θ, ϕ) space. We used the updated collimator transmission in this work.

2.4. Lunar surface chemistry

From the determined intensity ratios, geochemical maps of the surface can be reconstructed for the part of the Moon covered during each orbit. The resolution of the observations are approximately $60 \times 75 \text{ km}^2$ for the low-altitude orbits ($\sim 60 \text{ km}$) and $110 \times 125 \text{ km}^2$ for the high-altitude orbits ($\sim 110 \text{ km}$) when using the 8 sec measurements.

When constructing these maps, cuts were made to the data to remove noise and unreliable measurements. First, the intensity ratio data corresponding to the measured intensity by each detector that falls within 3σ of the average background were removed to reduce noise contributions. Second, all intensity ratios measured at times when the Sun was not in the FOV of the Solar monitor were cut from the data set since the X-rays measured at this point are dominated by scattered radiation. The first cleaning criterion removed $\sim 50\%$ of the XRFs data, while the second cleaning criterion removed $\sim 25\%$ of the XRFs data. Furthermore, during orbit 16 (July 31, 1971), 67 and 73 (August 4, 1971) of Apollo 15, and orbit 19 (April 21, 1972) of Apollo 16,

the Solar spectrum hardened, causing a decrease in all intensity ratios (Adler et al. 1972a; Bielefeld et al. 1977). These orbits (4.7% of total data) were taken out of the data set.

Since the Solar spectrum was softer during the Apollo 16 mission (see Sect. 2.3) with respect to that during the Apollo 15 mission, correction factors for the intensity ratios measured by Apollo 16 can be determined (see also Bielefeld 1977). The intensity ratio measurements of Apollo 15 and 16 of the same area on the Lunar surface can be compared by cross-matching the measurements and determining a linear fit, yielding correction factors of 0.95, 0.83, and 0.84 for the Apollo 16 Al/Si, Mg/Si, and Mg/Al measurements, respectively. Here we used the intensity ratios remaining after the cuts and before the mapping procedure further outlined in Sect. 3.

Detector #1 operated in the extended mode covering 1.4–6.0 keV for about 25% of the observation time (see Tab. 1). This mode enables one to measure the fluorescence from elements with higher atomic number elements, such as calcium (Ca) and iron (Fe). The $K\alpha$ line energies of Ca and Fe are 3.69 and 6.40 keV, respectively (e.g., Schoonjans et al. 2011). The Fe line can be detected in channel 8, which covers energies $>6 \text{ keV}$, and since the Fe line is broadened in the detector it can also partially be detected in channel 7. In using the same method as described above, maps of the intensity ratios, such as Ca/Si, Fe/Si, and

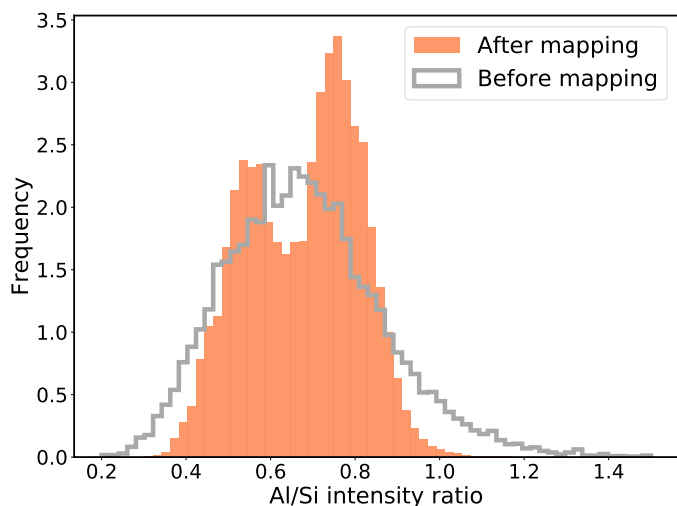


Fig. 3: Corrected normalized frequency distribution of Al/Si intensity ratio before and after mapping. The mapping before shows all 8 sec Al/Si intensity ratios measured by Apollo 15 & 16. The mapping after shows the frequency of the mean Al/Si intensity ratio stored on the constructed Lunar surface grid by taking the response into account.

Fe/Ca, can be constructed. Due to the limited amount of data taken in the extended mode, however, only a few percent of the Lunar surface was covered. Also, the count rates in the channels corresponding to Ca and Fe line intensities were low. The Ca/Si, Fe/Si, and Fe/Ca maps are therefore of low quality and are not discussed further.

3. Intensity ratio maps

We constructed Al/Si, Mg/Si, and Mg/Al intensity ratio maps of the Apollo 15 & 16 missions using the new collimator response and CSM orbit reconstruction. To visualize the X-ray intensity maps, a grid on the Lunar surface was constructed with a resolution of 0.1 degrees (~ 3 km) in longitude and latitude. The FOV was determined using the altitude at each 8 sec measurement and the newly determined collimator response. The rotation of the XRFS instrument with respect to the Lunar surface was also taken into account. For the creation of the Lunar maps, we used an equirectangular projection. We mapped the measured X-ray intensities onto the Lunar surface on each grid point and weighted the values with the transmission percentage. To include the 8 sec integration time, the transmission was smeared out over the distance traveled by the CSM, which was determined by interpolating the travel time between two following X-ray measurements. Finally, a weighted mean was determined for each point on the Lunar surface grid. Any points with only a single or no intensity ratio measurement with a higher than 20% transmission percentage have been excluded from the map.

The Al/Si intensity ratios on the Lunar surface measured by Apollo 15 and 16 are shown in Fig. 2. The map is projected onto an optical image of the Moon to investigate the location of certain geological features. The names of the known geological features are given in Appendix C in Fig. C.2. It is apparent from the map that the Lunar mare (dark) regions typically have lower Al/Si ratios than the Lunar highland (light) regions. The 1σ uncertainties of the Al/Si intensity ratios are displayed in the bottom panel of Fig. 2 and range from 0.01 to 0.36. It is important to note that the uncertainties on the Al/Si intensity ratios are es-

pecially high at the start and end of each track. This is likely to be caused by scattered light being more prominent than the fluorescent light due to Solar X-rays reaching the Lunar surface with a large angle and thus the total X-ray intensity being lower. Also, the data obtained near the terminator are less reliable due to poor counting statistics (Yin et al. 1993).

To quantify the distribution of the intensity ratios, we investigated the values as they were calculated and after they were stored on a grid of the Moon surface (i.e., "mapping"). The Al/Si distributions are shown in Fig. 3. The values before mapping are the intensity ratios calculated from each 8 sec measurement by Apollo 15 & 16 remaining after the applied data cuts (see Sect. 2.4). The intensity ratios after mapping are the mean intensity ratios on each grid point determined using the response of the collimator. Here it can be seen that after mapping, the Al/Si intensity ratio distribution is bimodal, which indicates the Lunar maria and highlands are clearly distinguishable, whereas before mapping this distinction could not be made.

The Mg/Si and Mg/Al intensity ratio maps are shown in Fig. 4. From these maps, it can be seen that the Lunar mare regions are characterized by higher Mg/Si and Mg/Al intensity ratios than the Lunar highlands. The intensity ratio distributions of Al/Si, Mg/Si, and Mg/Al with and without the correction factors for Apollo 16 (Section 2.3) are shown in Fig. 5. The corrections (right panel) result in additional peaks appearing in the Mg/Al and Mg/Si distributions, which is due to the relatively low values measured for Mg/Si and Mg/Al of the highland area between ~ 100 - 150 degrees longitude by Apollo 16. The relative peak height in the bimodal distribution of Al/Si and Mg/Al is caused by the relative amount of maria and highlands covered by the CSM. A bimodal Gaussian distribution fit gives mean Al/Si values with 1σ standard deviations of 0.54 ± 0.07 and 0.76 ± 0.07 with an Apollo 16 correction and 0.54 ± 0.07 and 0.78 ± 0.08 without corrections. The Mg/Al intensity ratio distributions are approximately bimodal with mean Mg/Al values of 0.54 ± 0.17 and 1.07 ± 0.13 with corrections and 0.57 ± 0.17 and 1.08 ± 0.12 without corrections. The Mg/Si intensity ratio is described by a single Gaussian distribution only, with a mean ratio of 0.47 ± 0.13 with corrections and 0.50 ± 0.13 without corrections. The Mg/Si data contain relatively more noise than the Al/Si data (see Clark 1979), which may contribute to the less apparent distinction between the geological features in the Mg/Si map. Finally, it should be noted that channel 1 of Detector #1 was noisy (see Clark 1979), which may contribute to the uncertainty in the intensity ratios.

4. Discussion & conclusion

We performed a re-evaluation of the Lunar orbit observations done by the X-ray Fluorescence Spectrometers onboard Apollo 15 & 16 using up-to-date knowledge of the detector, filters, and collimator transmission, as well as the CSM trajectory. This has resulted in updated Lunar surface maps of Al/Si, Mg/Si, and Mg/Al intensity ratios (see Fig. 2 and 4). These maps reveal Al-rich highlands and relatively Mg-rich maria, showing an inverse relationship between Al/Si and Mg/Si intensity ratios between the two types of terrain, as also stated in previous work (e.g., Adler et al. 1972a,b,c). We find, however, that our overall determined Al/Si intensity ratio values are $\sim 30\%$ lower than previously published (e.g., Adler et al. 1972a; Bielefeld et al. 1977; Andre et al. 1977). For example, in averaging the values in the region of Mare Tranquillitatis, we find an Al/Si intensity ratio of 0.52, whereas Bielefeld et al. (1977) found 0.75 and Adler et al. (1972a) found 0.81 ± 0.13 . Our intensity ratio maps are in agree-

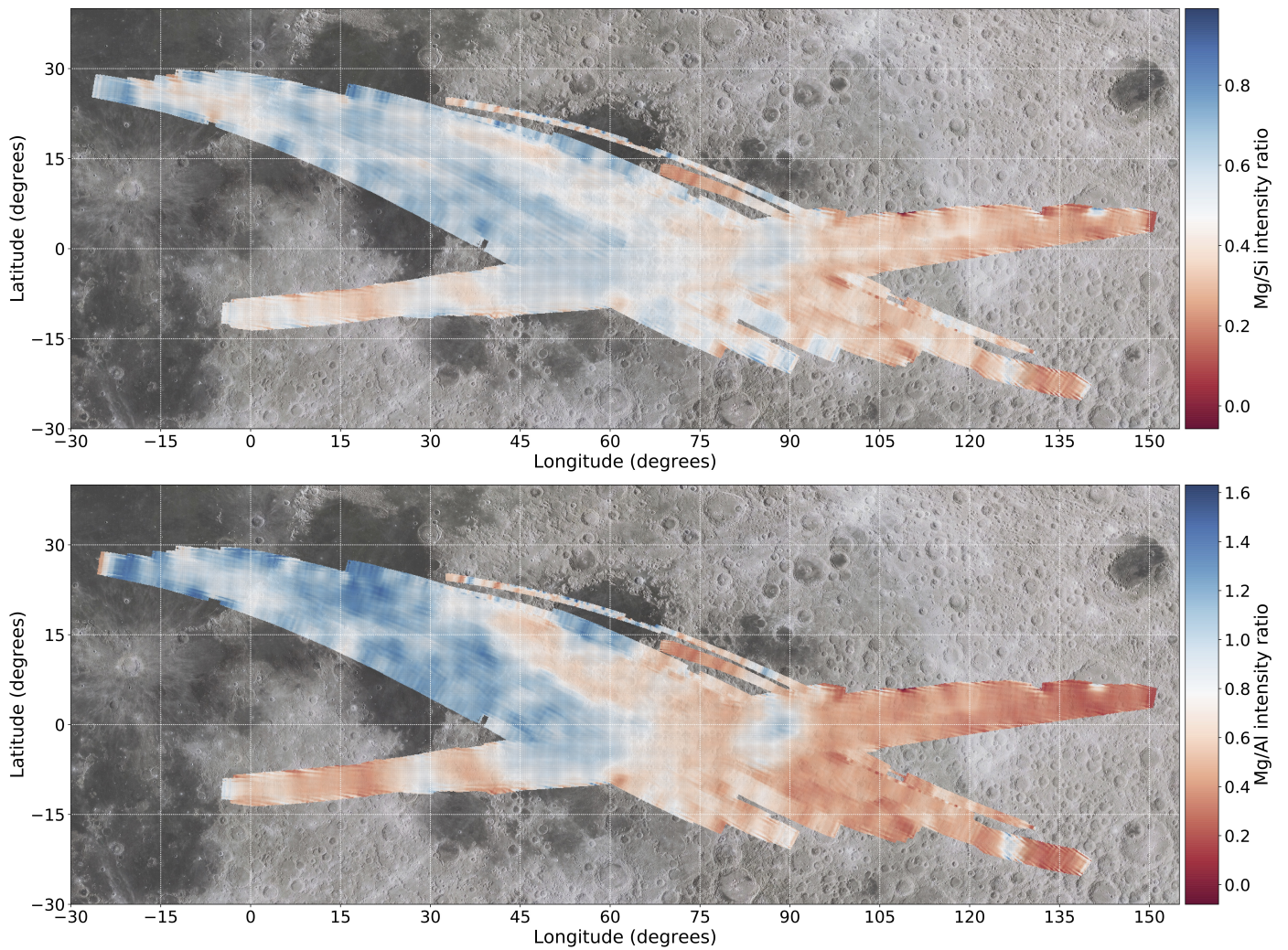


Fig. 4: Lunar surface maps of Mg/Si (top panel) and Mg/Al (bottom panel) intensity ratio measured from the Apollo 15 and 16 CSM projected onto an optical image of the Lunar surface.

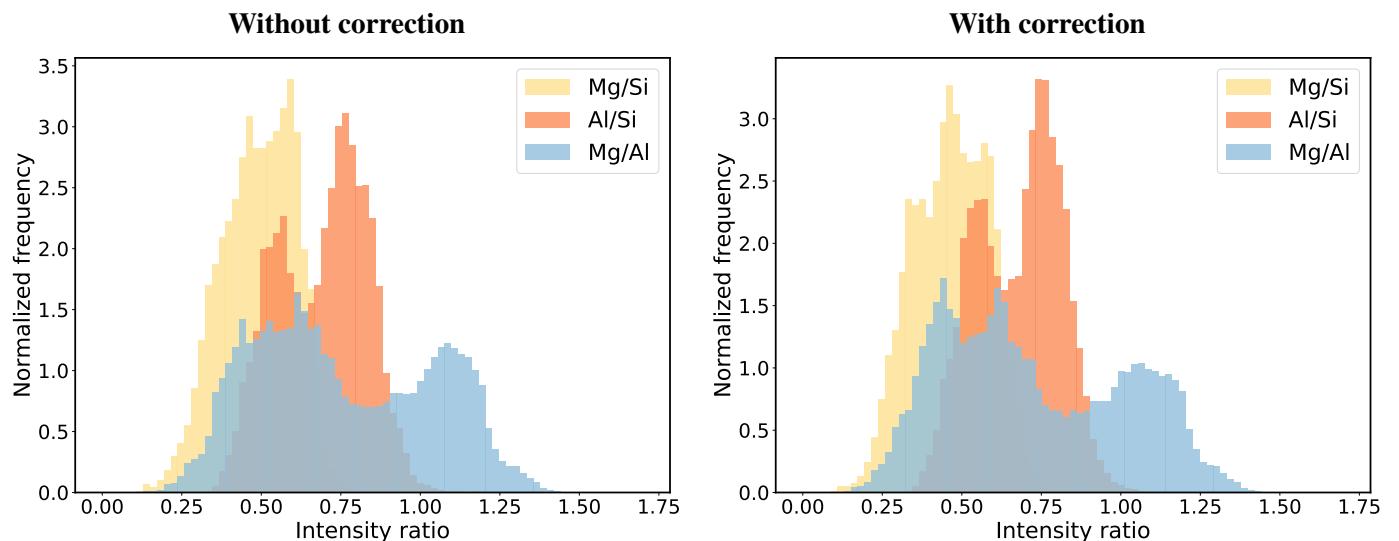


Fig. 5: Frequency distributions (normalized number of intensity ratios observed) of Al/Si, Mg/Si, and Mg/Al after mapping. Left: Distributions without correction of Apollo 16 data. Right: Distributions with Apollo 16 data corrected for softening of Solar spectrum. The corrections result in additional peaks appearing in the Mg/Al and Mg/Si distributions, which is due to the relatively low values measured for Mg/Si and Mg/Al of the highland area between ~ 100 – 150 degrees longitude by Apollo 16. In both figures, the intensity ratio bin width is approximately 0.02.

Table 3: Lunar rock samples concentration ratios obtained during Lunar missions compared to average observed X-ray fluorescence intensity ratios in this work.

Feature	Mission	Ref.	Rock type	Concentration ratio			Observed intensity ratio*		
				Al/Si	Mg/Si	Mg/Al	Al/Si	Mg/Si	Mg/Al
Mare Tranquillitatis	Apollo 11	[a]	High K rocks	0.23	0.24	1.04	0.52 ± 0.10	0.62 ± 0.15	1.15 ± 0.24
			Low K rocks	0.29	0.23	0.79			
	Surveyor V	[b]	Regolith	0.35					
Mare Fecunditatis	Luna 16	[c]	Rocks (average)	0.35	0.21	0.6	0.58 ± 0.13	0.51 ± 0.14	0.89 ± 0.29
Hadley-Apennines	Apollo 15	[d]	Fines (15021-80)	0.34	0.28	0.85	0.53 ± 0.19	0.64 ± 0.20	1.26 ± 0.30
Descartes Highlands	Apollo 16	[d]	Fines (61161-7)	0.67	0.18	0.26	0.81 ± 0.11	0.40 ± 0.14	0.49 ± 0.20
Taurus-Littrow	Apollo 17	[d]	Soil (72701-37)	0.52	0.28	0.54	0.55 ± 0.09	0.55 ± 0.12	1.01 ± 0.26

References: [a] [Levinson \(1970\)](#), [b] [Turkevich et al. \(1967\)](#), [c] [Vinogradov \(1971\)](#), [d] [Wänke et al. \(1973\)](#).

* Obtained in this work

ment with low-resolution global Lunar surface maps derived from the Chang'E-2 X-ray spectrometer ([Dong et al. 2016](#)).

The differentiation between mare and highland regions is clearly seen in the bimodal intensity ratio distribution (see Fig. 5). Furthermore, Lunar mare regions in general are characterized by higher Mg/Si and Mg/Al intensity ratios than the Lunar highlands, although this is less clear for the Mg/Si intensity ratio maps (see also, e.g., [Clark & Adler 1978](#); [Clark & Hawke 1981](#)). The comparatively higher Al/Si intensity ratio values in the highlands are due to the presence of anorthosite type rocks (mostly plagioclase feldspar). The mare regions, however, are characterized by high Mg/Si intensity ratio values compared to the highland regions due to relatively Mg-rich basaltic lavas, typically abundant in the mineral pyroxene (see, e.g., [Heiken et al. 1991](#)).

There are multiple methods that can be used to convert the observed intensity ratios into concentration ratios. Firstly, previous work has shown that there is a direct relationship between these measured intensity ratios and the concentration of the bulk soil ([Hubbard & King 1980](#)). Therefore, concentration ratios can be derived by combining remote sensing observations with Lunar sample investigations (see, e.g., [Adler et al. 1972a](#); [Trombka et al. 1977](#)), which can be directly determined through compositional analyses of samples from Lunar landing sites (e.g., [Heiken et al. 1991](#)). Secondly, the Solar spectrum can be reconstructed by comparing Solar observations in multiple energy bands to theoretical solar emission models, which can be used to determine the expected fluorescence. The relation between the hardness of the solar spectrum and expected fluorescence can then be used to correct the measured intensity ratios to concentrations (see e.g., [Hubbard et al. 1978](#); [Clark & Adler 1978](#); [Clark & Trombka 1997](#)). During the Apollo 15&16 missions, Solar observations were obtained by SOLRAD 10, which can also be used for this analysis (see e.g., [Clark & Adler 1978](#)). Finally, in the lab on the ground, element line intensity ratios can be directly related to element concentration ratios by experimentally measuring standards. We have not been able to find such calibration reports for the XRFS.

To obtain an estimate of the concentration ratios derived from our work, we compared our observed intensity ratios to concentration ratios obtained from Lunar samples from various missions in Tab. 3. The comparison between intensity ratio and concentration values can be used to generate an approximate calibration for these data. These values have been plotted in Fig. C.1 and are used to derive a linear relation between the measured intensity ratio and concentration ratio. Scaling the intensity ratios with these linear fits yields rough estimates for the concentration ratio of the mare and highland regions of 0.34 ± 0.11 and

0.71 ± 0.13 for Al/Si and 0.18 ± 0.19 and 0.77 ± 0.15 for Mg/Al, respectively. Again, no distinction can be made between the mare and highlands for the Mg/Si distribution; therefore, the distribution is described by a single Gaussian with a mean of 0.19 ± 0.08 .

In future studies an analysis of the measured Solar radiation itself can be used to construct a more accurate comparison between the Apollo 15 and Apollo 16 data, as well as inter-orbital variations during the individual missions (see, e.g., [Clark & Adler 1978](#); [Bielefeld et al. 1977](#)). These inter-orbital variations are largest for the Mg/Si ratio and are also partly caused by variations in surface roughness ([Hubbard & Keith 1977](#)). In addition, the differences in the instrument response and energy gain of Apollo 15 and 16 need further investigation to determine the correction needed for the Apollo 16 data. Also, the contribution from scattered X-ray photons needs to be disentangled from the pure fluorescent X-rays; this cannot be obtained from the Lunar data alone. The effect of scattered radiation is greatest on the Mg/Si intensity ratio since the exciting Solar flux strongly increases with energy and the Mg and Si line energies deviate the most ([Bielefeld 1977](#)). These extra corrections, together with a calibration to convert intensities to a concentration, will result in improved concentration maps, which can then finally be used to study the concentration ratios over an extended area of the Lunar surface and contribute to our current understanding of the Lunar surface geology and formation.

Acknowledgements. The authors thank the referee for the useful suggestions and comments. We are grateful to Bernard Foing, Juan García Redondo, and Francesca McDonald for the useful suggestions and discussions regarding this work. AJG and YM thank ESA/ESTEC and ESA/ESAC, respectively, for its hospitality during an internship. AE and MK acknowledge support from the ESTEC Faculty Visiting Scientist Programme. YM also acknowledges support from ESA through the Faculty of the European Space Astronomy Centre (ESAC) - Funding reference ESAC-357. EK thanks David R. Williams for making available the restored binary offline tape datasets from the NSSDC Archive and Gerald K. Austin for providing the XRFS Prototype Unit.

References

- Adler, I., Gerard, J., Trombka, J., et al. 1972a, Lunar and Planetary Science Conference Proceedings, 3, 2157
- Adler, I., Gorenstein, P., Trombka, J., et al. 2007, NASA Planetary Data System
- Adler, I., Schmadebeck, R., Trombka, J., Gorenstein, P., & Bjorkholm, P. 1975, Space Science Instrumentation, 1, 305
- Adler, I., Trombka, J., Gerard, J., et al. 1972c, Science, 175, 436
- Adler, I., Trombka, J., Gerard, J., et al. 1972b, in: Apollo 16 Preliminary Science Report, NASA SP-315, NASA Scientific and Technical Information Office, Washington, D.C., p. 19
- Adler, I., Trombka, J. I., Yin, L. I., et al. 1973, Naturwissenschaften, 60, 231
- Agostinelli, S., Allison, J., Amako, K., et al. 2003, Nuclear Instruments and Methods in Physics Research A, 506, 250
- Andre, C. G., Bielefeld, M. J., Eliason, E., et al. 1977, Science, 197, 986

- Bielefeld, M. J. 1977, Lunar and Planetary Science Conference Proceedings, 1, 1131
- Bielefeld, M. J., Andre, C. G., Eliason, E. M., et al. 1977, Lunar and Planetary Science Conference Proceedings, 1, 901
- Clark, P. E. 1979, PhD thesis, University of Maryland
- Clark, P. E. & Adler, I. 1978, in Lunar and Planetary Science Conference Proceedings, Vol. 9, 3029–3036
- Clark, P. E. & Hawke, B. R. 1981, in Lunar and Planetary Science Conference Proceedings, Vol. 12B, 727–749
- Clark, P. E. & Trombka, J. I. 1997, Journal of Geophysical Research: Planets, 102, 16361
- Dong, W.-D., Zhang, X.-P., Zhu, M.-H., Xu, A.-A., & Tang, Z.-S. 2016, Research in Astronomy and Astrophysics, 16, 4
- Foing, B., Racca, G., Marini, A., et al. 2006, Advances in Space Research, 37, 6, the Moon and Near-Earth Objects
- Golub, L., Bjorkholm, P., Harnden, F. R., Harris, B., & Gorenstein, P. 1972, ASE-3067, American Science and Engineering, Cambridge, MA
- Harrington, T. M., Marshall, J. H., Arnold, J. R., et al. 1974, Nuclear Instruments and Methods, 118, 401
- Heiken, G., Vaniman, D., & French, B. M. 1991, S&T, 82, 498
- Henke, B., Gullikson, E., & Davis, J. 1993, Atomic Data and Nuclear Data Tables, 54, 181
- Hubbard, N. & Keith, J. 1977, in Lunar and Planetary Science Conference Proceedings, Vol. 8, 909–923
- Hubbard, N. & King, B. S. 1980, in Lunar Highlands Crust, ed. R. B. Merrill & J. J. Papike, 457–466
- Hubbard, N. J., Vilas, F., & Keith, J. E. 1978, in Lunar and Planetary Science Conference, Vol. 9, 558–560
- Jagoda, N., Kubierschky, K., Frank, R., Bjorkholm, P., & Gray, P. 1974, IEEE Transactions on Nuclear Science, 21, 194
- Kamata, Y., Takeshima, T., Okada, T., & Terada, K. 1999, Advances in Space Research, 23, 1829
- Levinson, A. A. 1970, Geochimica et Cosmochimica Acta Supplement, 1
- Narendranath, S., Athiray, P. S., Sreekumar, P., et al. 2011, Icarus, 214, 53
- Nittler, L. R., Starr, R. D., Lim, L., et al. 2001, Meteoritics & Planetary Science, 36, 1673
- Nittler, L. R., Starr, R. D., Weider, S. Z., et al. 2011, Science, 333, 1847
- Okada, T., Shirai, K., Yamamoto, Y., et al. 2007, in Lunar and Planetary Science Conference, 1287
- Racca, G. D., Foing, B. H., & Coradini, M. 2001, Earth Moon and Planets, 85, 379
- Schlemm, C. E., Starr, R. D., Ho, G. C., et al. 2007, Space Sci. Rev., 131, 393
- Schmitt, J. H. M. M., Snowden, S. L., Aschenbach, B., et al. 1991, Nature, 349, 583
- Schoonjans, T., Brunetti, A., Golosio, B., et al. 2011, Spectrochimica Acta Part B: Atomic Spectroscopy, 66, 776
- Trombka, J. I., Arnold, J. R., Adler, I., Metzger, A. E., & Reedy, R. C. 1977, Lunar elemental analysis obtained from the Apollo gamma-ray and X-ray remote sensing experiment., Vol. 370, 153–182
- Trombka, J. I., Gorenstein, P., Gursky, H., et al. 2007, NASA Planetary Data System
- Turkevich, A. L., Franzgrote, E. J., & Patterson, J. H. 1967, Science, 158, 635
- Vinogradov, A. P. 1971, in Lunar and Planetary Science Conference Proceedings, Vol. 2, 1
- Wänke, H., Baddenhausen, H., Dreibus, G., et al. 1973, Lunar and Planetary Science Conference Proceedings, 4, 1461
- Wargelin, B. J., Markevitch, M., Juda, M., et al. 2004, ApJ, 607, 596
- Weider, S. Z., Nittler, L. R., Starr, R. D., et al. 2015, Earth and Planetary Science Letters, 416, 109
- Yin, L. I., Trombka, J. I., Adler, I., & Bielefeld, M. 1993, in: Remote Geochemical Analysis: Elemental and Mineralogical Composition, 199

Appendix A: Filter thickness

The thickness of the Mg and Al filters, as well as that of the Be windows, is not entirely clear from the literature as different values have been published (e.g., Adler et al. 1972a; Adler et al. 1975; Clark 1979; Yin et al. 1993). The Mg and Al filter thickness is, for example, stated to be in the range of 5.08–12.7 μm in Adler et al. (1972a), while values of 5.1 and 6.4 μm are given by Clark (1979) and Yin et al. (1993), respectively. The Be window thickness is quoted as $\sim 25 \mu\text{m}$ in most work (e.g., Adler et al. 1972a; Adler et al. 1975; Clark 1979; Yin et al. 1993; Clark & Trombka 1997); however, for example, it is 40 μm in Adler et al. (1973). It should be noted that the resulting intensity ratios highly depend on the assumed window and filter thickness since this determines the amount of X-ray transmission.

An attempt to determine the correct thickness of the Al and Mg filter can be made. The filter transmission can be estimated from the XRFS observations of, for example, the bright X-ray source Scorpius X-1 during the trans-Earth coast flight obtained by Apollo 15 on August, 5 1971. By using the ratios of overall detected counts in each channel of Detectors #3 and #1 (Al/no filter) and Detectors #2 and #1 (Mg/no filter), the effect of the Be window was divided out when the thickness of the Be window was assumed to be the same for all three detectors. The background in each channel during the trans-Earth coast flight was determined from observations taken before and after the Scorpius X-1 measurement when the cover was open. The resulting transmission as a function of channel energy is shown in Fig. A.1. This method does not favor a thickness of 5.1 or 6.4 μm for either filter, but it does seem to rule out a thickness of 12.7 μm . We note that the Al transmission in the first channel is too high for either filter thickness, which may be due to instrumental noise in that channel of Detector #1 (see Clark 1979). Furthermore, we measured the filter thickness on the XRFS prototype unit (see Sect. 2.3); however, due to exposure to air during their storage, these filters have been affected, hence yielding inaccurate measurements. In this work, we therefore adopted the Be window thickness and Al & Mg filters thickness (see Tab.2) as published in Clark & Adler (1978), Clark (1979) and Yin et al. (1993).

Appendix B: Filter transmission

In this section, the determination of Al, Si, and Mg intensities as discussed in Sect. 2.3 is further explained. Equation 1 in its complete form is given by (see, e.g., Adler et al. 1972a):

$$\begin{aligned} G_1 &= I_{\text{Mg}}^T T_{\text{Mg}}^{\text{Be}} F_{1\text{Mg}} + I_{\text{Al}}^T T_{\text{Al}}^{\text{Be}} F_{1\text{Al}} + I_{\text{Si}}^T T_{\text{Si}}^{\text{Be}} F_{1\text{Si}}, \\ G_2 &= I_{\text{Mg}}^T T_{\text{Mg}}^{\text{Be}} F_{2\text{Mg}} + I_{\text{Al}}^T T_{\text{Al}}^{\text{Be}} F_{2\text{Al}} + I_{\text{Si}}^T T_{\text{Si}}^{\text{Be}} F_{2\text{Si}}, \\ G_3 &= I_{\text{Mg}}^T T_{\text{Mg}}^{\text{Be}} F_{3\text{Mg}} + I_{\text{Al}}^T T_{\text{Al}}^{\text{Be}} F_{3\text{Al}} + I_{\text{Si}}^T T_{\text{Si}}^{\text{Be}} F_{3\text{Si}}. \end{aligned} \quad (\text{B.1})$$

In these equations, G_i are the background subtracted counts in detector i for $i = 1, 2, 3$. Furthermore, I^T is the total flux at the Mg, Al, or Si $K\alpha$ line energy, T_j^{Be} is the transmission efficiency of the Be window, and F_{ij} is the transmission efficiency of each detector's i at the Al, Si, and Mg $K\alpha$ line energies (given by j). The transmission efficiencies of the Be, Mg, and Al filter are given by the exponential function $e^{-\mu_i \rho d_i}$, with μ being the absorption cross section, ρ being the density, and d being the thickness of the filter (see Equations 2, 3, and 4). Filling out

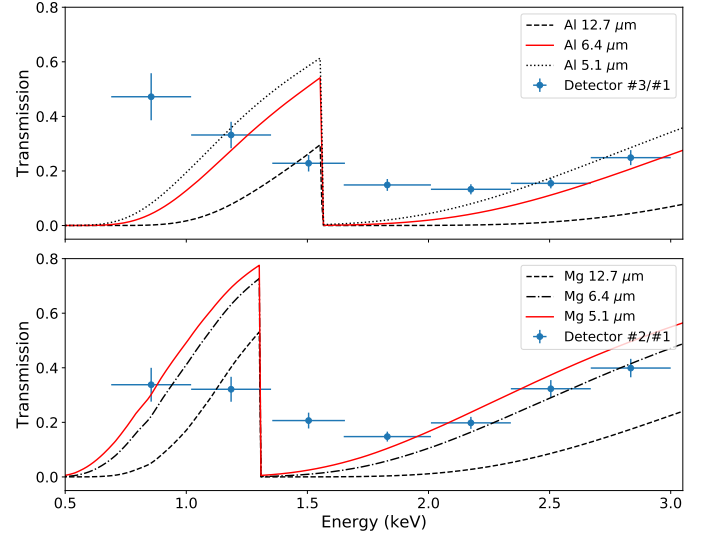


Fig. A.1: Transmission of the Al (Detector #3/#1, top) and Mg (Detector #2/#1, bottom) filter when observing Scorpius X-1 during the trans-Earth coast flight of Apollo 15. Filter transmission of Al (top) and Mg (bottom) is given as a function of energy for different thicknesses obtained from http://henke.lbl.gov/optical_constants/ (Henke et al. 1993).

the values of these constants as given in Tab. 2 results in a filter matrix M of

$$\begin{aligned} M &= \begin{bmatrix} T_{\text{Mg}}^{\text{Be}} F_{1\text{Mg}} & T_{\text{Al}}^{\text{Be}} F_{1\text{Al}} & T_{\text{Si}}^{\text{Be}} F_{1\text{Si}} \\ T_{\text{Mg}}^{\text{Be}} F_{2\text{Mg}} & T_{\text{Al}}^{\text{Be}} F_{2\text{Al}} & T_{\text{Si}}^{\text{Be}} F_{2\text{Si}} \\ T_{\text{Mg}}^{\text{Be}} F_{3\text{Mg}} & T_{\text{Al}}^{\text{Be}} F_{3\text{Al}} & T_{\text{Si}}^{\text{Be}} F_{3\text{Si}} \end{bmatrix} \\ &= \begin{bmatrix} e^{-(\mu_{\text{Be}}^{\text{Mg}} \rho_{\text{Be}} d_{\text{Be}})} & e^{-(\mu_{\text{Be}}^{\text{Al}} \rho_{\text{Be}} d_{\text{Be}})} \\ e^{-(\mu_{\text{Be}}^{\text{Mg}} \rho_{\text{Be}} d_{\text{Be}} + \mu_{\text{Mg}}^{\text{Mg}} \rho_{\text{Mg}} d_{\text{Mg}})} & e^{-(\mu_{\text{Be}}^{\text{Al}} \rho_{\text{Be}} d_{\text{Be}} + \mu_{\text{Mg}}^{\text{Al}} \rho_{\text{Mg}} d_{\text{Mg}})} \\ e^{-(\mu_{\text{Be}}^{\text{Mg}} \rho_{\text{Be}} d_{\text{Be}} + \mu_{\text{Al}}^{\text{Mg}} \rho_{\text{Al}} d_{\text{Al}})} & e^{-(\mu_{\text{Be}}^{\text{Al}} \rho_{\text{Be}} d_{\text{Be}} + \mu_{\text{Al}}^{\text{Al}} \rho_{\text{Al}} d_{\text{Al}})} \end{bmatrix} \quad (\text{B.2}) \\ &= \begin{bmatrix} 0.2373 & 0.4222 & 0.5857 \\ 0.1520 & 0.0113 & 0.0496 \\ 0.0774 & 0.2073 & 0.0027 \end{bmatrix}. \end{aligned}$$

It is important to note that this filter matrix is almost identical, as can be deduced from values given by Yin et al. (1993). Finally, the equation given by

$$\begin{bmatrix} G_1 \\ G_2 \\ G_3 \end{bmatrix} = M \begin{bmatrix} I_{\text{Mg}}^T \\ I_{\text{Al}}^T \\ I_{\text{Si}}^T \end{bmatrix} \quad (\text{B.3})$$

was solved to obtain I_{Mg}^T , I_{Al}^T , and I_{Si}^T . Once these three intensities were obtained, the Al/Si, Mg/Si, and Mg/Al intensity ratios were given by $I_{\text{Al}}^T/I_{\text{Si}}^T$, $I_{\text{Mg}}^T/I_{\text{Si}}^T$, and $I_{\text{Mg}}^T/I_{\text{Al}}^T$, respectively. The residuals obtained from the least square inversion method are negligible. Instead, Poisson statistics (square root of the number of counts) were used to estimate the uncertainty in the intensity ratios.

Appendix C: Rock concentration and geological features

Fig. C.1 shows the intensity ratios versus rock concentration ratios from Tab. 3. These linear fits were used to give an estimate for the mean measured concentration ratios (see Sect. 4). Fig. C.2 gives the geological names of the most prominent Lunar features covered by the Apollo 15 and 16 XRFS experiment.

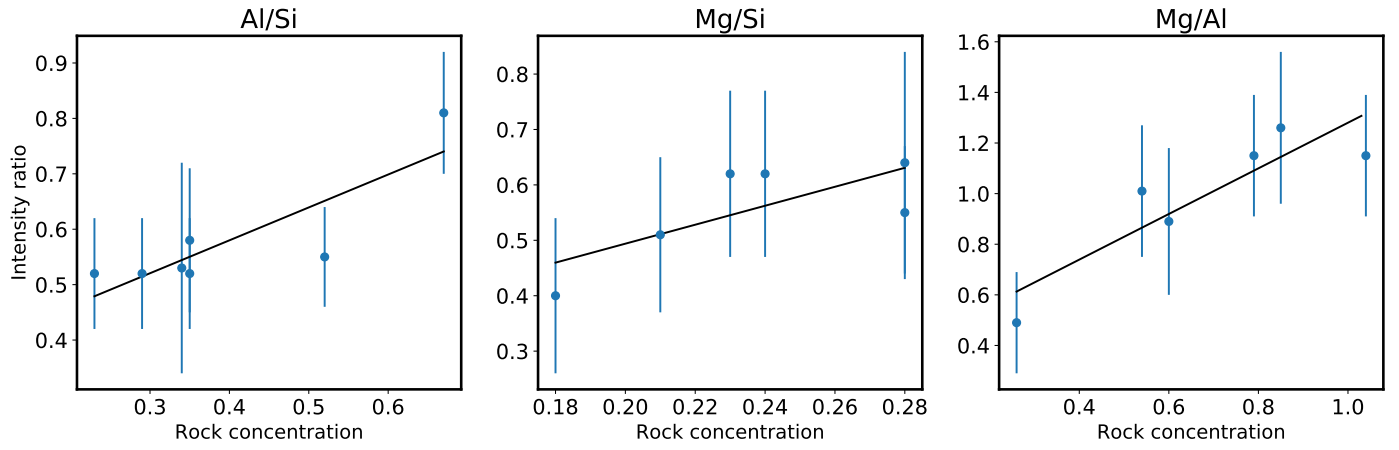


Fig. C.1: Intensity ratio as a function of the measured Lunar rock concentration of Al/Si (left), Mg/Si (middle), and Mg/Al (right) from Tab. 3 with the black line showing the optimal linear fits.

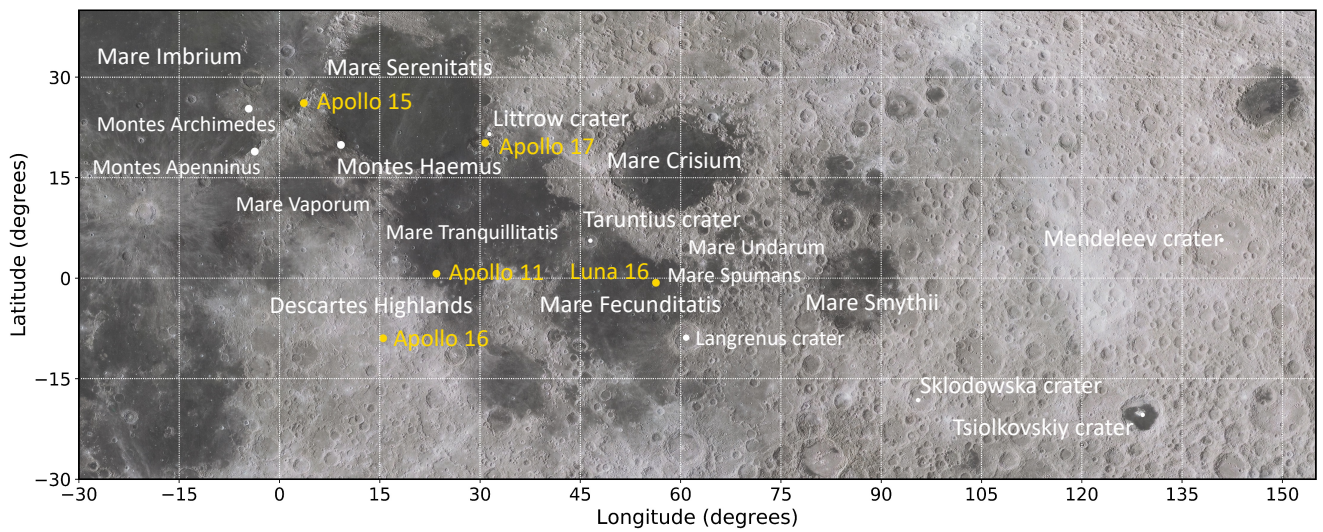


Fig. C.2: Map of Lunar surface with names of geological features. The landing site of Apollo 11, 15, 16, 17, and Luna 16 are given in yellow.